KSME

Springer

Journal of Mechanical Science and Technology 36 (10) 2022

Original Article
DOI 10.1007/s12206-022-0915-y

Keywords:
· Fe-based shape memory alloy
· Microhardness
· Corrosion resistance
· Shape recovery rate

Correspondence to:
Peng Xu
pxu2@gzu.edu.cn;
Chi Pang
p-chi@flyboat365.com

Citation:
Liu, X., Xu, P., Yao, L., Li, X., Pang, C., Yang, L., Liang, Y. (2022). Nb reinforced Fe-Mn-Si shape memory alloy composite coating fabricated by laser cladding on 304 stainless steel surface. Journal of Mechanical Science and Technology 36 (10) (2022) 5027~5033.
http://doi.org/10.1007/s12206-022-0915-y

Received March 19th, 2022
Revised April 27th, 2022
Accepted June 14th, 2022

† Recommended by Editor Chongdu Cho

Nb reinforced Fe-Mn-Si shape memory alloy composite coating fabricated by laser cladding on 304 stainless steel surface

Xiaochen Liu[1], Peng Xu[1,2], Like Yao[1], Xiang Li[1], Chi Pang[1], Long Yang[2] and Yi Liang[3]

[1]College of Materials and Metallurgy, Guizhou University, Guiyang 550025, China, [2]Guizhou Huake Aluminium Co., Ltd., Guiyang 550014, China, [3]School of Foreign Languages, Guizhou Normal University, Guiyang 550001, China

Abstract Laser cladding technology was adapted to fabricate Fe-based shape memory alloy/Nb composite coatings with 5 wt. % Nb doping amounts on 304 stainless steel to promote the microhardness and wear resistance. The SEM, XRD, optical profilometer and electrochemical workstation were used to characterize micromorphology, phase and microstructure. Meanwhile, wear and anti-resistance ability were detected. The results showed that Nb, NbC, ε-martensite, α'-martensite and γ-austenite were found in SMA/Nb coating. The microhardness was enhanced because of the solid solution strengthening and second phase strengthening. Also, the shape recovery rate and anti-corrosion property of the SMA/Nb coating are improved as well.

1. Introduction

Nowadays, 304 stainless steel is in widespread use, such as the chemical industry, marine environments and nuclear industry because of its excellent corrosion and heat resistance [1, 2]. However, the rapid development of science, technology and severe service conditions put forward higher demands for its wear resistance, corrosion resistance and hardness [3]. Laser cladding possesses the advantages of controllable dilution rate of cladding layer and small thermal deformation of substrate [4, 5] and is generally used to improve material surface properties [6]. Nevertheless, the partial high energy input and sheer gradients lead to grave residual stress [7, 8]. The residual stress may lead to crack formation in the coating [9] and reduce mechanical and anti-corrosion properties. More seriously, it even causes workpiece cracking [10], which affects the use of the workpiece gravely.

Currently, preheating substrate method and stress relief annealing are generally used to eliminate the residual stress [11-13]. Besides, Robinson [14] adopted the cold compression method to remove the residual stress on 7050 aluminum alloy. Experiment results signified that the residual stress on the three directions of XYZ decreases significantly after cold compression. But these methods have a complex process and high production costs. Because the Fe-Si-Mn SMA has stress self-accommodation characteristic (residual stress induction γ-austenite → ε-martensite [15]), which can release the residual stress and it has attracted researchers' attention recently. Xu [16] successfully fabricated FeNiCrSiMn SMA coating on 304 stainless steel surface by utilizing laser cladding, which not only weaken residual stress but have favorable wear resistance and anti-corrosion property. However, the microhardness of 260 $HV_{0.2}$ and corrosion resistance ability cannot meet the practical application.

In order to enhance the anti-corrosion ability and microhardness of the coating, laser cladding technology was used to manufacture Nb doped SMA composite coating. The microstructure, microhardness, corrosion resistance, wear resistance and shape memory recovery rate of the SMA/Nb coating was characterized and made a comparison with those of the SMA coating.

2. Materials and methods

2.1 Materials and sample preparation

The substrate is 304 stainless steel sheets (5 cm * 3 cm * 0.8 cm). The dirt and oxides are removed by polishing to ensure the cleanliness of the substrate. The composition was demonstrated in Table 1.

The composition of cladding powder is consisting of Nb, Fe, Ni, Cr, Si and Mn (purity > 99 %, power size 50-100 μm) as shown in Table 2 and the electronic balance (mettler toledo) was used to weigh powders. Then dried for 2 h using a QM-3SP2 ball mill at 25 °C. The laser system (YLS6000) and powder preparation process are shown in Figs. 1(a) and (b). The optimal parameters were displayed below: laser power of P = 2 kW, the scanning rate of v = 6 mm/s and pre-sintered powder thickness is 1.5 mm.

2.2 Characterization methods

The samples were cut with a dimension of 7 mm * 7 mm * 7 mm by using wire electrical discharge machining and polished after cutting. An optical microscope (CSW-E200M) and an SEM (COXEM, EM30) were used to characterize the micromorphology and chemical composition. The energy dispersive spectrometer (EDS) (OXFORD INSTRUMENT) was employed to observe element distribution. The X-ray diffractometer (DX-2700B) (Using Cu Kα target and the diffraction angle (2θ) varied from 10° to 90° at a scanning rate of 0.03°/s.) was employed to characterize phase composition.

HSR-2M reciprocating friction tester and Vickers microhardness tester were utilized to take measurements of wear resistance and microhardness. The load was 10 N; the diameter of the steel ball was 3 mm; the test time was 15 minutes and the reciprocating distance was 4 mm.

The optical profilometer (ContourGT-X3, Bruker, Germany) was used to analyze surface morphology. The three-electrode system of electrochemical workstation (CHI604D; CH Instruments Company, Ltd. The area of Pt electrode is 1 cm^2) was used for measuring polarization curves and Nyquist plots in 3.5 % sodium chloride solution at 25 °C.

Table 1. Chemical composition of 304 stainless steel.

Fe	Ni	Cr	Si	Mn	C
Bal.	8 %-15 %	18 %-20 %	≤ 1.00 %	≤ 2.00 %	≤ 0.08 %

Table 2. Powder composition of laser cladding.

Composition	Fe	Si	Cr	Mn	Nb	Ni
wt. %	52	9	4	32	0	3
wt. %	49.4	8.55	3.8	30.4	5	2.85

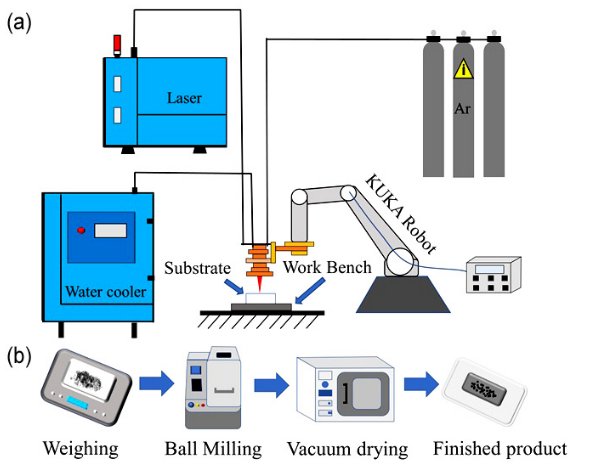

Fig. 1. Schematic diagram of (a) fiber laser system; (b) powder sample.

2.3 Shape memory recovery

To determine the shape recovery rate, samples were cut into a dimension of 40 mm * 2.5 mm * 0.5 mm using wire electrical discharge machining. The samples were experienced solution-treatment for 1 hour at 1000 °C, and the recovery rate is estimated by bending test, as shown in Fig. 2. First, the sample is bent 180° at room temperature then unloaded, elastic recovery angle θ_e was measured in the meantime. Then it was kept at 800 °C for 1 hour (γ-austenite → ε-martensite transformation temperature), and the recovery angle θ_m was measured in the meantime. The recovery rate was calculated as shown in Eq. (1).

$$\eta = \theta_m / (180° - \theta_e) . \quad (1)$$

3. Results and discussion

3.1 Microstructure and phase composition

Fig. 3(a) displays the XRD spectrums of the three samples and Fig. 3(b) presents the magnified of 46°-48° range. The transformation of austenite will generate α'-martensite and ε-martensite, where α'-martensite weakens the shape memory effect [17], so we should avoid it as much as possible. Else, the

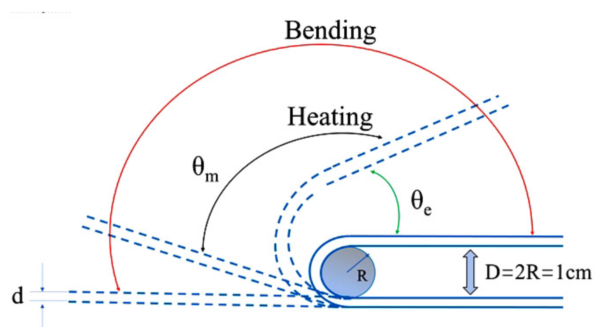

Fig. 2. Schematic diagram of bending and recovery experiment.

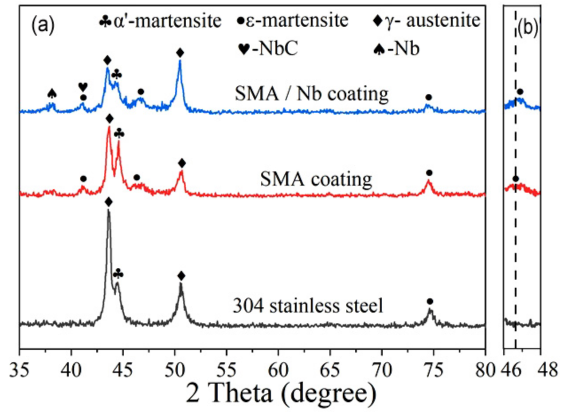

Fig. 3. XRD patterns for (a) the SMA coating, SMA/Nb composite coating and 304 stainless steel; (b) the enlarged of 45°-48°range in (a).

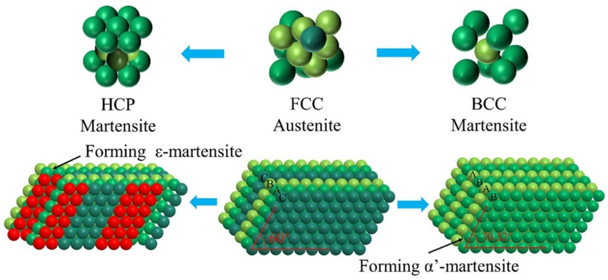

Fig. 4. Changes in atomic arrangement during phase transformation.

α'-martensite in the substrate may be formed during polishing. The experimental data in Fig. 3(a) reveals that martensite transformation (γ → ε) was induced by residual stress in the experiment process because the ε-martensite and γ-austenite exist in SMA coating and SMA/Nb coating. Furthermore, X-ray diffraction spectrums show that a second phase NbC was produced in SMA/Nb coating, which leads to the second phase strengthening. Fig. 3(b) exhibits that the peak position of the ε phase with 2θ = 46.62° shifted slightly to the right, owing to the lattice distortion caused by Nb atoms which entered the lattice and solid solution strengthening.

Fig. 4 reveals the transformed atomic arrangement of transformation γ → ε+α'. The essence of martensite transformation is the variation of crystal structure caused by atomic slip and α'-martensite is sheared in terms of the classical K-S relationship [18].

Fig. 5(a) demonstrates the interface presents fine metallurgical bonding and Fig. 5(b) displays the microstructure of the SMA/Nb coating. The microstructure distribution displays as planar, cellular, columnar dendritic and equiaxed dendritic. Each region of the microstructure can be explained by the composition undercooling theory and the morphology is mainly affected by the factors G and R [19]. G and R present temperature gradient and solidification rate respectively. The heat removal rate at the interface between the subtract and SMA/Nb coating is relatively poor, leading to big temperature gradient G and small solidification rate R. There is almost no composition

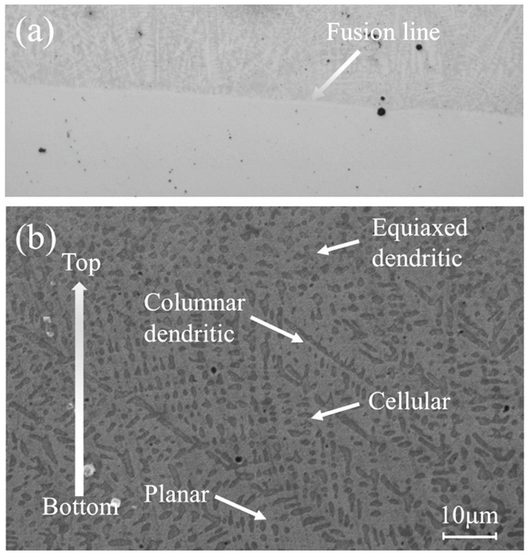

Fig. 5. Metallographic photographs of the fused layer from top to bottom.

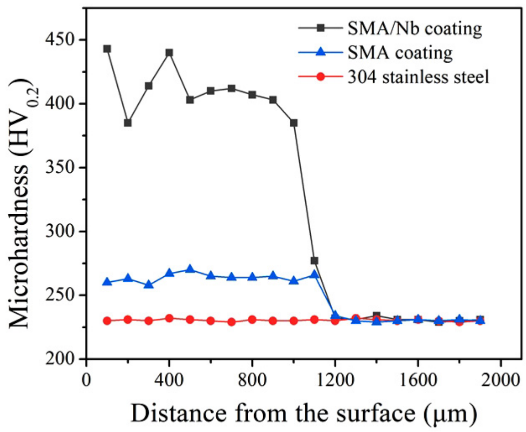

Fig. 6. Microhardness distribution of SMA/Nb composite coating, SMA coating and 304 stainless steel.

undercooling region, so it is characterized by plane crystal [20]. With the solidification of the SMA/Nb coating, G decreases and R increases. Therefore, the microstructure is subsequently presented as cellular, columnar dendritic, and equiaxed dendritic.

3.2 Microhardness

As demonstrated in Fig. 6, the microhardness of composite coating has been dramatically improved over 1.5 times. The improvement of microhardness of composite coatings owing to the double roles of solid solution strengthening and second phase strengthening. In XRD analysis, it was found that the diffraction peak shifted to a big angle, indicating that Nb atoms entered the cell and led to solid solution strengthening. In addition, a small amount of NbC was also found in the SMA/Nb coating, which rose the function of the second phase strengthening [21]. Moreover, NbC can hinder dislocation movement and play a pinning role in the substrate [22], contributing greatly to the hardness of SMA/Nb coating as well.

3.3 Wear resistance

Wear resistance can be characterized by the size and stability of the friction coefficient curves. In general, small and stable friction coefficient curves delegate to better wear resistance. Clearly, the SMA/Nb coating has the smallest friction coefficient, about 1/3 of the substrate and 2/5 of the SMA coating as shown in Fig. 7(a). Furthermore, the wear resistance can be estimated through the wear volume loss as well. Fig. 7(b) presents the volume loss of the SMA/Nb coating is only 0.1 mm^3, which is much lower than the 0.6 mm^3 and 0.22 mm^3 of the substrate and SMA coating. It illustrates that SMA/Nb coating has the best wear resistance. High microhardness and perfect wear resistance are compatible with Archard's tribological theory [23].

The contour of the wear regions of the three coatings were presented in Fig. 8(a), Fig. 8(b) is the morphology of the wear region, (c)-(k) are the EDS analysis in Fig. 8(b), respectively. Evidently, the wear track of the composite coating is narrower and smoother, which proves that the SMA/Nb coating has better wear resistance.

Fig. 8(b) presented the morphology of the wear region. Adhesive wear can be judged to have occurred because the metal on the surface is peeled off [24]. In the wear resistance test, the mill ball has compressive stress and shear stress on the surface area. As displayed in Fig. 8(b), the surface broke when plastic deformation reached fracture peak [25]. The EDS of the abrade section was carried out as in Figs. 8(c)-(k), indicating that Nb and O elements are widely distributed in the wear region and the presence of compound Nb_2O_5 can be inferred. Nb_2O_5 has strong plasticity [26] and soft texture, which is easy to induce adhesive wear.

Meanwhile, the friction between the mill ball and the sample will increase the surface temperature in the wear resistance test. Studies have shown that the hardness of the composite coating will decrease [27] and the wear mechanism has a tendency to turn to adhesive wear when the temperature increases [28].

3.4 Corrosion resistance

The polarization curves of the three samples are exhibited in Fig. 9(a), and Table 3 presents polarization curves data. The SMA/Nb coating has the highest E_{corr} but the I_{corr} increased compared with SMA coating, which presents the composite coating has the weakest corrosion thermodynamic trend [29] and the corrosion resistance of the composite coating was enhanced [30]. The corrosion resistance was improved because the heterogeneous nucleation of Nb atoms as alien crystal nucleus, resulting in grain refinement. And Nb element par-

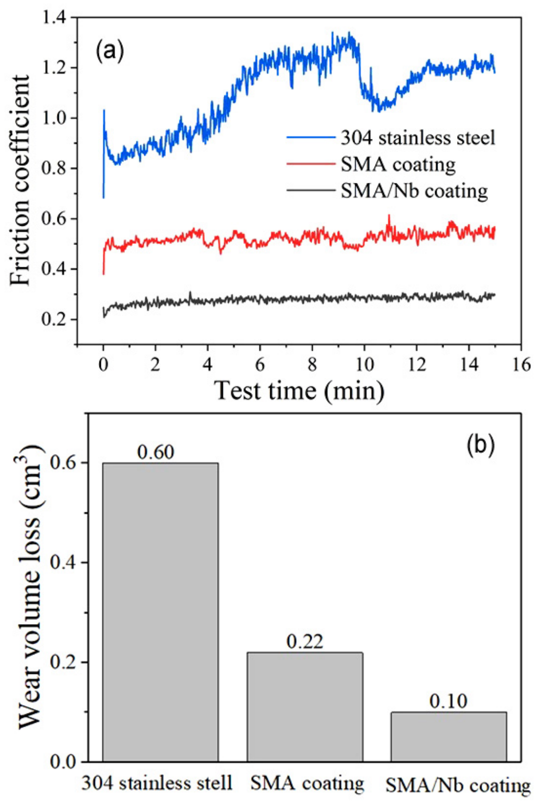

Fig. 7. Friction coefficient curves: (a) wear volume loss; (b) of SMA/Nb composite coating, SMA coating and 304 stainless steel.

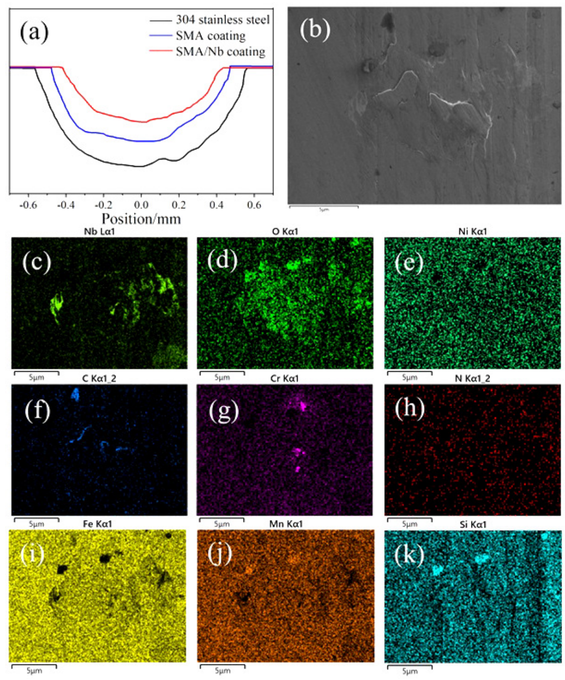

Fig. 8. (a) Contour of the wear regions of the three coatings; (b) morphology of wear region; (c)-(k) EDS surface scanning of SMA/Nb composite coating.

Table 3. Polarization curve parameters of samples.

Material	E_{corr} (V)	I_{corr} (A/cm^2)
SMA/Nb coating	-1.23	3.17×10^{-5}
SMA coating	-1.25	3.03×10^{-5}
304 stainless steel	-1.31	3.75×10^{-5}

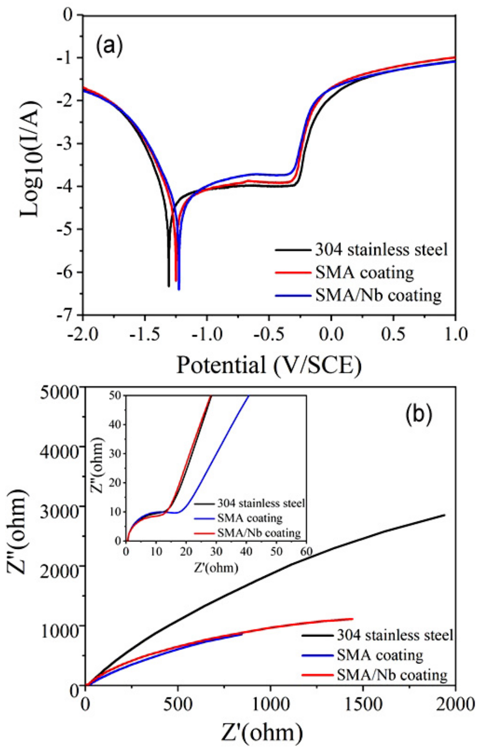

Fig. 9. (a) Polarization curves of SMA/Nb composite coating, SMA coating and 304 stainless steel; (b) the Nyquist plots of the three coatings.

Table 4. Data of shape recovery test.

	304 stainless steel	SMA coating	SMA/Nb coating
θ_e	18°	20°	17°
θ_m	0°	2°	5°
η	0 %	1.25 %	3.07 %

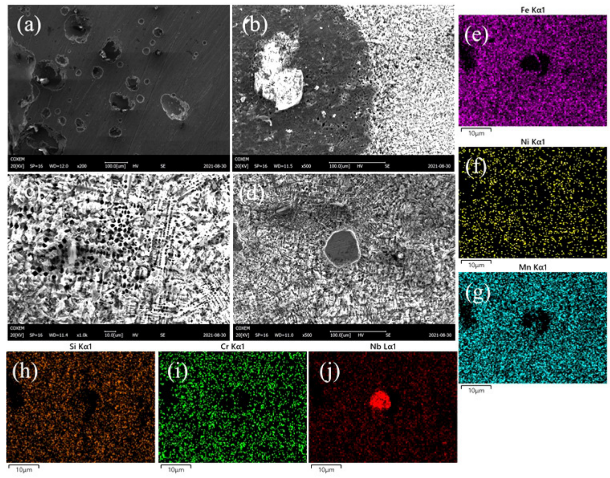

Fig. 10. (a)-(d) the corrosion morphology of 304 stainless steel, SMA coating and SMA/Nb composite coating; (e)-(j) are the distribution of Fe, Mn, Si, Cr, Nb and Ni elements in (d).

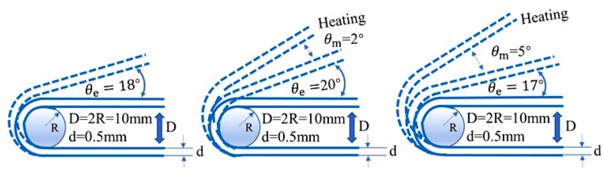

(a) 304 stainless steel (b) Nb = 0 wt.% (c) Nb = 5 wt.%

Fig. 11. Recoveries of memory alloy coatings with different Nb contents: (a) 304 stainless steel; (b) Nb = 0 wt.%; (c) Nb = 5 wt.%.

ticipates in the formation of passivation region in the corrosion process [31], thus reducing intergranular corrosion.

The Nyquist plots of three samples were presented in Fig. 10. The Nyquist plot curve is related to the corrosion rate [32] and large diameters stand for the better the corrosion resistance [33]. As shown in Fig. 9(b) that the radius of SMA coating is lightly larger than that of SMA/Nb coating and substrate at the initial corrosion period, indicating that the impedance of SMA coating is the largest at the initial period.

After the beginning of corrosion, the radius of the substrate is the largest, which shows that the substrate has the largest impedance and SMA/Nb has the smallest impedance. This is because the Cr element is very essential for the anti-corrosion property. Moreover, the content of Cr element determines the corrosion resistance as shown in Eq. (2) [34].

$$\begin{aligned} \text{PRE(PREN)} &= \text{Pitting Resistance Equivalence Number} \\ &= \%Cr + 3.3\,\%Mo + 16\,\%N \end{aligned} \tag{2}$$

The Cr element in the substrate is 18-20 wt.%, which is much higher than that of SMA/Nb coating (3.8 wt.%) and SMA coating (4.0 wt. %), so the impedance of 304 stainless steel is the largest.

Fig. 10(a) presents the SEM image of the sample. Compared with the substrate and SMA coating, SMA/Nb coating has dissimilar corrosion types. As displayed in Fig. 10(a), the extensive of pitting corrosion occurred on the substrate surface, which greatly weakened the mechanical properties. The data presented in (b)-(d) show that the large area of corrosion happened in composite coating and SMA coating, and the corrosion morphology shows a large area of holes. Besides, Nb element aggregation occurred in the SMA/Nb coating, after doping Nb element, as shown in Figs. 10(e)-(j).

3.5 Shape recovery rate

Fig. 11 shows schematic diagrams of shape recovery rate and the test data are shown in Table 4. The pre-deformation d/D = 0.5 mm/10 mm = 5 %. The shape recovery rate of SMA/Nb coating is 3.07 % as shown in Fig. 11, which is significantly higher than SMA coating. This can be explained by the XRD pattern that NbC was formed in the SMA/Nb coating and it can provide a favorable position for martensite nucleation during stress-induced ε-martensitic transformation. Other authors obtained the same results as well [35].

4. Conclusions

1) Microhardness and wear resistance of the SMA/Nb coating have been dramatically upgraded owing to the second phase strengthening and solid solution strengthening. The microhardness of the SMA/Nb coating has been enhanced 1.5 times. The friction coefficient is about 2/5 of 304 stainless steel and 2/3 of SMA coating. Moreover, the fluctuation of the friction coefficient is obviously lower than that of the substrate and SMA.

2) The anti-corrosion ability of SMA/Nb coating was improved and the corrosion voltage increased from -1.31 V to -1.23 V. Meanwhile, the shape recovery rate of the SMA/Nb coating has been dramatically enhanced.

Acknowledgments

This study was funded by SRT Project of Guizhou University ([2021]003), Guizhou Provincial Science and Technology Foundation (QKHJC ZK [2021] general 241), Guizhou Provincial Science and Technology Achievements Transformation Project (QKHCG [2021] general 112), Natural Science Research Project of Guizhou Provincial Education Department (QJH KY Z [2021]098) and Fostering Projects of Guizhou University ([2020]66).

References

[1] D. Li et al., Enhancement of wear resistance by sand blasting-assisted rapid plasma nitriding for 304 austenitic stainless steel, *Surf. Eng.*, 36 (2020) 524-530.

[2] N. G. Krishna et al., Surface modification of type 304 stainless steel with duplex coatings for corrosion resistance in sea water environments, *Surf. Eng.*, 31 (2015) 39-47.

[3] L. J. Song et al., Repair of 304 stainless steel by laser cladding with 316L stainless steel powders followed by laser surface alloying with WC powders, *J. Manuf. Process.*, 24 (2016) 116-124.

[4] S. T. Sun et al., Effect of CeO_2 addition on microstructure and mechanical properties of in-situ (Ti, Nb) C/Ni coating, *Surf. Coat. Tech.*, 359 (2019) 300-313.

[5] G. Muvvala et al., In-process detection of microstructural changes in laser cladding of in-situ Inconel 718/TiC metal substrate composite coating, *J. Alloy. Compd.*, 740 (2018) 545-558.

[6] L. Lucia et al., On the influence of laser cladding parameters and number of deposited layers on as-built and machined AISI H13 tool steel multilayered claddings, *CIRP. J. Manuf. Sci. Tec.*, 35 (2021) 361-370.

[7] Tamanna et al., A numerical investigation of similar and dissimilar clad materials on H13 steel substrate in the laser cladding process, *Adv. Mater. Process. Tec.*, 5 (2019) 598-606.

[8] M. S. Ghorashi et al., Considering cyclic plasticity to predict residual stresses in laser cladding of Inconel 718 multi bead samples, *J. Manuf. Process.*, 42 (2019) 149-158.

[9] D. Z. Wang et al., Residual stress and cracking behaviors of Cr13Ni5Si2 based composite coatings prepared by laser-induction hybrid cladding, *Surf. Coat. Tech.*, 274 (2015) 51-59.

[10] Y. F. Tao et al., Residual stress distribution in different depths of TiNi/Ti2 Ni-based laser clad coating prepared at different environmental temperatures, *T. Nonferr. Metal. Soc.*, 27 (2017) 2043-2054.

[11] H. Ali et al., Residual stress development in selective laser-melted Ti6Al4V: a parametric thermal modelling approach, Int. *J. Adv. Manuf. Tech.*, 97 (2018) 2621-2633.

[12] W. Ya et al., Cladding of Tribaloy T400 on steel substrates using a high power Nd: YAG laser, *Surf. Coat. Tech.*, 350 (2018) 323-333.

[13] C. Courbon et al., Near surface transformations of stainless steel cold spray and laser cladding deposits after turning and ball-burnishing, *Surf. Coat. Tech.*, 371 (2019) 235-244.

[14] J. S. Robinson et al., Residual stress relief in the aluminium alloy 7075, *Mater. Sci. Tech-Lond.*, 33 (2017) 1765-1775.

[15] C. Bellini et al., A cyclic integrated microstructural-mechanical model for a shape memory alloy, *Int. J. Fatigue.*, 153 (2021) 106473.

[16] P. Xu et al., In-situ synthesis of Fe-Mn-Si-Cr-Ni shape memory alloy functional coating by laser cladding, *Chin. Opt. Lett.*, 12 (2014) 52-54.

[17] T. Maki, Microstructure, mechanical property and shape memory effect or ferrous martensite, *Shanghai Mentals.*, 15 (1993) 1-7.

[18] S. Morito et al., The morphology and crystallography of lath martensite in Fe-C alloys, *Acta. Mater.*, 51 (2003) 1789-1799.

[19] W. Q. Li et al., Microstructure evolution and mechanical properties of 308L stainless steel coatings fabricated by laser hot wire cladding, *Mat. Sci. Eng. A-Struct.*, 824 (2021) 141825.

[20] Z. H. Tian et al., Microstructure and properties of Inconel 625 + WC composite coatings prepared by laser cladding, *Rare Metals.*, 40 (2021) 2281-2291.

[21] B. Zhang et al., Laser surface alloying with carbon on 15-5PH steel for improved wear resistance, *Surf. Eng.*, 37 (2021) 669-677.

[22] X. L. Ping, Microstructure and performance of Nb-bearing Ni60A-Cr_3C_2 coatings manufactured by laser cladding, *Surf. Eng.*, 36 (2020) 1294-1306.

[23] J. B. Cheng et al., Nb doping in laser-cladded $Fe_{25}Co_{25}Ni_{25}(B_{0.7}Si_{0.3})_{25}$ high entropy alloy coatings: microstructure evolution and wear behavior, *Surf. Coat. Tech.*, 402 (2020) 126321.

[24] Y. X. Guo and Q. B. Liu, MoFeCrTiWAlNb refractory high-entropy alloy coating fabricated by rectangular-spot laser cladding, *Intermetallics*., 102 (2018) 78-87.

[25] W. Xu et al., Microstructure, wear resistance, and corrosion performance of Ti35Zr28Nb alloy fabricated by powder metallurgy for orthopedic applications, *J. Mater. Sci. Technol.*, 41 (2020) 191-198.

[26] S. Guo et al., Wear response of metastable β-type Ti-25Nb-2Mo-4Sn alloy for biomedical applications, *Rare Metals.*, 34 (2015) 564-568.

[27] J. Z. Shao et al., Microstructure and wear behaviors of TiB/TiC reinforced Ti2Ni/α (Ti) matrix coating produced by laser cladding, *Rare Metals.*, 39 (2020) 304-315.
[28] Y. G. Meng et al., A review of recent advances in tribology, *Friction*, 8 (2020) 221-300.
[29] H. Z. Wang et al., Microstructure and properties of laser clad Fe-based amorphous alloy coatings containing Nb powder, *J. Non-cryst. Solids.*, 550 (2020) 120351.
[30] S. C. Tao et al., Microstructure, mechanical properties and antibacterial properties of the microwave sintered porous Ti–3Cu alloys, *J. Alloy. Compd.*, 812 (2019) 152142.
[31] W.R. Wang et al., Microstructure and corrosion behavior of $(CoCrFeNi)_{95}Nb_5$ high-entropy alloy coating fabricated by plasma spraying, *Materials.*, 12 (2019) 694-706.
[32] X. Shi et al., Corrosion resistance and biocompatibility of calcium-containing coatings developed in near-neutral solutions containing phytic acid and phosphoric acid on AZ31B alloy, *J. Alloy. Compd.*, 823 (2020) 153721.
[33] X. He et al., Microstructure and corrosion behaviours of composite coatings on S355 offshore steel prepared by laser cladding combined with micro-arc oxidation, *Appl. Surf. Sci.*, 497 (2019) 143703.
[34] U. K. Mudali and B. Raj, *High Nitrogen Steels and Stainless Steels: Manufacturing, Properties and Applications*, Asm. International (2004) 148.
[35] Z. Z. Dong et al., Effect of pre-deformation at room temperature on shape memory properties of stainless type Fe-15Mn-5Si-9Cr-5Ni-(0.5-1.5) NbC alloys, *Acta. Mater.*, 53 (2005) 4009-4018.

Xiaochen Liu is an undergraduate student at Guizhou University and his major is Materials Science and Engineering. He joined Prof. Xu's group in 2020. His current research interest focuses on Shape Memory Alloy.

Peng Xu received his Ph.D. in Dalian Maritime University. He is currently an Associate Professor in the college of materials and metallurgy, Guizhou university. His research interest mainly focuses on Shape memory alloy, Additive manu- facturing, Lithium sulfur battery.

Like Yao is an undergraduate student majoring in Materials Science and Engineering at Guizhou University. He joined Prof. Xu's group in his sophomore year. His research direction is laser cladding and metal heat treatment.

Pang Chi was born in 1975 and received his Master's degree in Xidian University. He is an Associate Professor in the College of Materials and Metallurgy, Guizhou University. His research subjects are Additive manufacturing and ZnO piezoelectric ceramics.

Xiang Li is a junior student at Guizhou University, majoring in Materials Science and Engineering. He joined Prof. Xu's group in his sophomore year and his research directions focus on Surface Modification and Shape Memory Alloy.